

Sensitivity of SKA to dark matter induced radio emission

Zhanfang Chen,^{1,2} Yue-Lin Sming Tsai,^{1,*} and Qiang Yuan^{1,2}

¹*Key Laboratory of Dark Matter and Space Astronomy,*

Purple Mountain Observatory, Chinese Academy of Sciences, Nanjing 210033, China

²*School of Astronomy and Space Science,*

University of Science and Technology of China, Hefei, Anhui 230026, China

(Dated: August 12, 2021)

Abstract

Conventionally, one can constrain the dark matter (DM) interaction with DM mass heavier than GeV by searching for DM induced synchrotron emission in the radio frequency band. However, an MeV DM can also generate detectable radio emission if electrons and positrons produced by DM annihilation or decay undergoes inverse Compton scattering (ICS) with the cosmic microwave background. The upcoming radio telescope Square Kilometre Array (SKA) is designed to operate with extremely high sensitivity. We investigate the capability of the SKA to detect DM particles in a board mass range from MeV to TeV, for both annihilation and decay scenarios. In this paper, we consider the sensitivities of the future SKA first and second phase (SKA1 and SKA2). As a comprehensive study, we systematically study the impacts on the DM-induced signal computation from the magnetic field strengths and particle diffusion coefficients. We compare the detection potential of four very different sources: two dwarf spheroidal galaxies (Draco and Segue 1), one radio-poor cluster (A2199), and one DM-rich ultra-diffuse galaxy (Dragonfly 44). We project the SKA1 and SKA2 sensitivities with the exposure of 100 hours on the annihilation cross section and decay time for DM mass from MeV to TeV by considering two different leptonic final states e^+e^- and $\mu^+\mu^-$.

* smingtsai@pmo.ac.cn

I. INTRODUCTION

The anisotropies in the cosmic microwave background show that around a quarter of the Universe consists of dark matter (DM). However, the existence of DM is only revealed by its gravitational interaction with visible matter. Nevertheless, people do not yet discard the assumption that DM might interact with visible matter via non-gravitational interactions. After decades of efforts to search for non-gravitational interactions between DM and visible matter, significant progress has been reached, such as the underground DM direct detection experiments [1, 2], colliders [3, 4], or photon and cosmic ray observations known as DM indirect detection [5–7]. The sensitivities of these measurements have been improved rapidly in recent years, especially for the DM mass greater than 10 GeV. Therefore, the direction of the future DM searches of non-gravitational interactions should aim for either the lighter DM mass region or the extremely weak coupling region. These regions require detectors with a smaller threshold energy or larger exposure.

Compared with collider and direct detection, the strategy of DM indirect detection can be more flexible by looking for different targets or using various telescopes with very different threshold energy. Taking the γ -ray telescope as an example, the Fermi Gamma-ray Space Telescope has reported the current best limits of DM annihilation cross section ($b\bar{b}$ final state) for DM mass around 60 GeV [8] based on a combined analysis of 15 dwarf galaxies (dSphs). The strongest constraint in the TeV mass range is given by the ground-based telescopes HESS through the observation of the Galactic Center [9]. The future ground-based telescopes Cherenkov Telescope Array (CTA) [10] can significantly improve the sensitivity and probe the thermal DM cross section $\langle\sigma v\rangle \simeq 10^{-26} \text{ cm}^3\text{s}^{-1}$ for DM mass between 200 GeV and 10 TeV.

If the standard model electrons and positrons are produced by DM annihilation or decay, they may lose their energies either by inverse Compton scattering (ICS) with the Cosmic microwave background (CMB) photons or synchrotron radiation from gyration in the magnetic field, and radiate in the radio frequencies. Both ICS and synchrotron emission can contribute to this frequency, depending on the DM mass. If DM mass is heavier than GeV, the synchrotron emission can be detected by current or future radio telescopes [11–13]. For DM mass smaller than 100 MeV, the peak frequency of the DM synchrotron emission is too low to be detected. However, one can still observe DM ICS within the radio frequency

range [14]. A recent deep radio observation of the dSph Reticulum II with the Australia Telescope Compact Array shows a competitive limit for DM masses between 10 GeV to 100 GeV [15]. Similar studies are also performed by Ref. [16] with the Green Bank Telescope, by Ref. [17] with the combined data from the Murchison Widefield Array and the Giant Metre-wave Radio Telescope, and by Ref. [18] with a stacking analysis of 23 dSph galaxies using data from TIFR GMRT Sky Survey.

The Square Kilometre Array (SKA) is a planned radio telescope array, which will be built in Australia and South Africa. The first phase of SKA, known as SKA1, is going to start its construction in 2021. The frequency coverage of the SKA is from 50 MHz to 50 GHz. The outstanding resolution and sensitivity of the SKA could effectively probe GeV scale DM via synchrotron emission [19, 20]. A recent study [21] also shows that the multi-lepton anomalies at the LHC [22] may be probed by future observations of Reticulum II. Some recent studies [19, 20] have estimated that the SKA sensitivity on the annihilation cross section of DM with masses heavier than GeV. For DM mass range below GeV, the ICS emission is shown to be more relevant than the synchrotron emission [14]. The SKA sensitivity is also discussed in probing the DM induced synchrotron radiation from the DM-rich Ultra-faint Dwarf Galaxies [23]. In this work, we estimate the SKA sensitivities on DM annihilation cross section and decay rate in a wide mass range from MeV to TeV. Both the ICS and synchrotron emission caused by either DM annihilation or decay are considered. We study comprehensively the impacts of the poorly unknown magnetic field strengths and diffusion coefficients. We also discuss the detectability based on four different sources (Segue1, Draco, A2199, and Dragonfly 44) with different properties.

The SKA1 sensitivity has been investigated for both the DM induced synchrotron [19–21, 24–26] and ICS [14] in the literature, but it can be more useful to consistently consider them together from MeV to TeV. For example, the present works of SKA sensitivity for DM induced synchrotron are mainly focusing on DM mass greater than 5 GeV [19–21, 24–26]. On the other hand, the SKA sensitivity for the DM induced ICS is only presented based on DM mass less than 100 MeV [14] for DM annihilation and decay to e^+e^- final state. Therefore, our work fills the mass gap between 100 MeV to 5 GeV and we compute both synchrotron and ICS emission with a consistent model configuration. Our work shows that the synchrotron contribution is equally important as ICS one in this mass gap. Comparing with the DM ICS limits in Ref. [14], we include not only e^+e^- final state but also the $\mu^+\mu^-$

channel.

The paper is organized as follows. In Sec. II, the SKA sensitivity is briefly described. We discuss the two phases of SKA1 and SKA2. In Sec. III, we recap the derivation of radio SED and show its variation when changing the magnetic field strength and diffusion coefficient. In the last part of Sec. III, we also survey using different sources. In Sec. IV, we present the upper limits of DM annihilation cross section and DM decay rate based on SKA1 and SKA2 sensitivity, assuming no radio emission is detected. We summarize our results in Sec. V.

II. THE SQUARE KILOMETRE ARRAY

The SKA is designed to detect radio in the range between 50 MHz to 50 GHz. The strongest strength of the SKA lies in its high sensitivity and energy resolution. Particularly, the detection of dSphs will benefit from the SKA strength because dSphs usually are faint radio sources. Some recently developed telescopes such as the Green Bank Telescope (GBT) and the Australia Telescope Compact Array (ATCA) make radio observations of several dSphs [15–17]. In these studies, null-detection have been observed and their sensitivities of radio emission is $\approx \mathcal{O}(\text{mJy})$ ($\sim 10^{-26} \text{ erg}\cdot\text{cm}^2\cdot\text{s}^{-1}\cdot\text{Hz}^{-1}$). In the near future, we expect that the SKA array would detect radio emission with the sensitivities of $\mathcal{O}(\mu\text{Jy})$ [27].

The minimum flux detected by the SKA telescope can be obtained by the following equation [20]:

$$S_{\min} = \frac{2k_b S_D T_{\text{sys}}}{\eta_s A_e (\eta_{\text{pol}} \mathcal{T} \Delta\nu)^{1/2}}, \quad (1)$$

where k_b represents the Boltzmann constant, η_s represents the system efficiency, and η_{pol} is the number of polarisation states. A degradation factor for the noise in a continuum image is denoted as $S_D = 2$. In our work, the channel bandwidth $\Delta\nu$ is adopted as 0.3 times the frequency [29]. On the other hand, a fixed value $\Delta\nu = 300 \text{ MHz}$ is used in Ref. [14, 20, 23, 25]. This difference makes our S_{\min} larger (smaller) than others at the lower (higher) frequency regions. The minimum flux is related to the effective collecting area A_e divided by the total system noise temperature T_{sys} . The change of the ratio A_e/T_{sys} with frequency can be found in Fig. 7 of Ref. [28]. Here, \mathcal{T} represents the total integration time.

The first SKA phase (SKA1) can detect a minimum flux $3 \times 10^{-21} \text{ erg cm}^{-2}\text{s}^{-1}$ for \mathcal{T} equal to 100 hours at 1 GHz. However, for the second SKA phase (SKA2), the minimum

energy flux could be lowered down to $\approx 3 \times 10^{-22}$ erg cm $^{-2}$ s $^{-1}$. In the following sections, we will discuss both the SKA1 and SKA2 sensitivities for DM annihilation cross section and decay rate.

III. DM RADIO EMISSION AND ENERGY SPECTRUM DISTRIBUTION

One of most likely radio origins may be DM, because its annihilation or decay to the relativistic electrons and positrons produce the radio emission via synchrotron for $m_\chi > \mathcal{O}(100 \text{ MeV})$ or inverse Compton (IC) for $m_\chi < \mathcal{O}(100 \text{ MeV})$. In this section, we start with the analytical solution of the electron and positron propagation equation. A simple assumption is that the electrons and positrons propagate with no convection, no reacceleration, and a very large time scale for fragmentation and radioactive decay. Hence, a simple propagation equation can be written as

$$-\nabla \left[D(E, \mathbf{r}) \nabla \frac{\partial n_e}{\partial E} \right] - \frac{\partial}{\partial E} \left[b(E, \mathbf{r}) \frac{\partial n_e}{\partial E} \right] = Q(E, \mathbf{r}), \quad (2)$$

where the source term of DM annihilation/decay is

$$Q_e(E, r) = \begin{cases} \frac{1}{2} \left[\frac{\rho(r)}{m_\chi} \right]^2 \langle \sigma v \rangle \frac{dN_e}{dE} & \text{for DM annihilation,} \\ \frac{\rho(r)}{m_\chi} \times \frac{1}{\tau} \times \frac{dN_e}{dE} & \text{for DM decay.} \end{cases} \quad (3)$$

The annihilating DM properties are described by the DM mass m_χ , velocity averaged annihilation cross section $\langle \sigma v \rangle$, normalized DM annihilation energy spectrum $\frac{dN_e}{dE}$ and DM halo profile density ρ . For decaying DM, the decay time τ is inversely proportional to decay rate. Note that $Q_e(E, r)$ is proportional to $\left[\frac{\rho(r)}{m_\chi} \right]^2$ for annihilating DM while $\frac{\rho(r)}{m_\chi}$ for decaying DM.

During the propagation, the electrons and positrons interact with the interstellar medium gas, CMB, and galactic magnetic fields. The diffusion coefficient can be modeled as

$$D(E) = D_0 \times E^\gamma, \quad (4)$$

where we take $\gamma = 0.3$ for the Kolmogorov description. According to the study of the measured B/C ratio data in the Milky Way, the diffusion coefficient D_0 ranges from 10^{27} to 10^{29} cm 2 s $^{-1}$ [30, 31].

The energy loss term $b(E, \mathbf{r})$ accounts the total energy loss via synchrotron, IC, Coulomb, and bremsstrahlung processes. The explicit form of the energy loss term is

$$\begin{aligned} b(E, \mathbf{r}) &= b_{\text{IC}}(E) + b_{\text{syn.}}(E, \mathbf{r}) + b_{\text{coul.}}(E) + b_{\text{brem.}}(E) \\ &= b_{\text{IC}}^0 E^2 + b_{\text{syn.}}^0 B^2(r) E^2 + b_{\text{coul.}}^0 n_e \left[1 + \log \left(\frac{E/m_e}{n_e} \right) / 75 \right] \\ &\quad + b_{\text{brem.}}^0 n_e \left[\log \left(\frac{E/m_e}{n_e} \right) + 0.36 \right], \end{aligned} \quad (5)$$

where n_e represents the average thermal electron density. In this work, we take $n_e = 10^{-3} \text{cm}^{-3}$ for A2199 [39] and $n_e = 10^{-6} \text{cm}^{-3}$ for Segue1, Draco, and DF44 [32]. Following Ref. [24, 32], we simply take the energy loss factors $b_{\text{IC}}^0 = 0.25$, $b_{\text{syn.}}^0 = 0.0254$, $b_{\text{coul.}}^0 = 6.13$, and $b_{\text{brem.}}^0 = 1.51$ in units of 10^{-16}GeV/s . Moreover, the averaged values of magnetic field of four sources are $0.0880 \mu\text{G}$ (Draco), $0.0475 \mu\text{G}$ (Segue1), $3.57 \mu\text{G}$ (A2199), and $0.432 \mu\text{G}$ (DF44). Here, the magnetic field and plasma densities are averaged within the diffusion zone.

For the boundary condition, the positron density is generally assumed to vanish at the boundary of the diffusive zone. In terms of the Green's function $G[\mathbf{r}, \lambda(E, \varepsilon)]$, the solution arising from Eq. (2) is

$$\frac{\partial n_e}{\partial E}(E, \mathbf{r}) = \frac{1}{b(E, \mathbf{r})} \int_E^{m_x} d\varepsilon G[\mathbf{r}, \lambda(E, \varepsilon, \mathbf{r})] Q(\mathbf{r}, \varepsilon). \quad (6)$$

The mean free path of e^\pm is denoted as λ ,

$$\lambda^2(E, \varepsilon, \mathbf{r}) = 4 \int_E^\varepsilon \frac{D(\varepsilon')}{b(\varepsilon', \mathbf{r})} d\varepsilon' \quad (7)$$

with the e^\pm energy ε' before the propagation. Note that Green's function must vanish on the edge of leaking box due to boundary condition. Therefore, we can simply apply the method of image charges to obtain the Green function. With the *image charge* of each real charge, we can sum of real charges and all its image charges at the position $r_n = (-1)^n r + 2nr_h$. Each charge can be treated as free-space Green functions,

$$G[\mathbf{r}, \lambda(E, \varepsilon, \mathbf{r})] = \sum_{n=-\infty}^{\infty} (-1)^n G_{\text{free}}(\mathbf{r}, \lambda), \quad (8)$$

where a free-space Green function¹ is given by

$$G_{\text{free}}[\mathbf{r}, \lambda(E, \varepsilon, \mathbf{r})] = \frac{1}{\sqrt{\pi\lambda^2}} \int_0^{r_n} dr' \frac{r'}{r_n} \left[\frac{\rho(r')}{\rho(r)} \right]^\alpha \times \left[e^{-\frac{(r'-r_h)^2}{\lambda^2}} - e^{-\frac{(r'+r_h)^2}{\lambda^2}} \right]. \quad (9)$$

¹ Instead of using the image charge method, another method proposed by Ref. [33] shows that the Green function can be expanded by a Fourier series. We have confirmed that the maximum difference between two numerical results is around 50%.

Again, the index α is for either decaying DM $\alpha = 1$ or annihilating DM $\alpha = 2$.

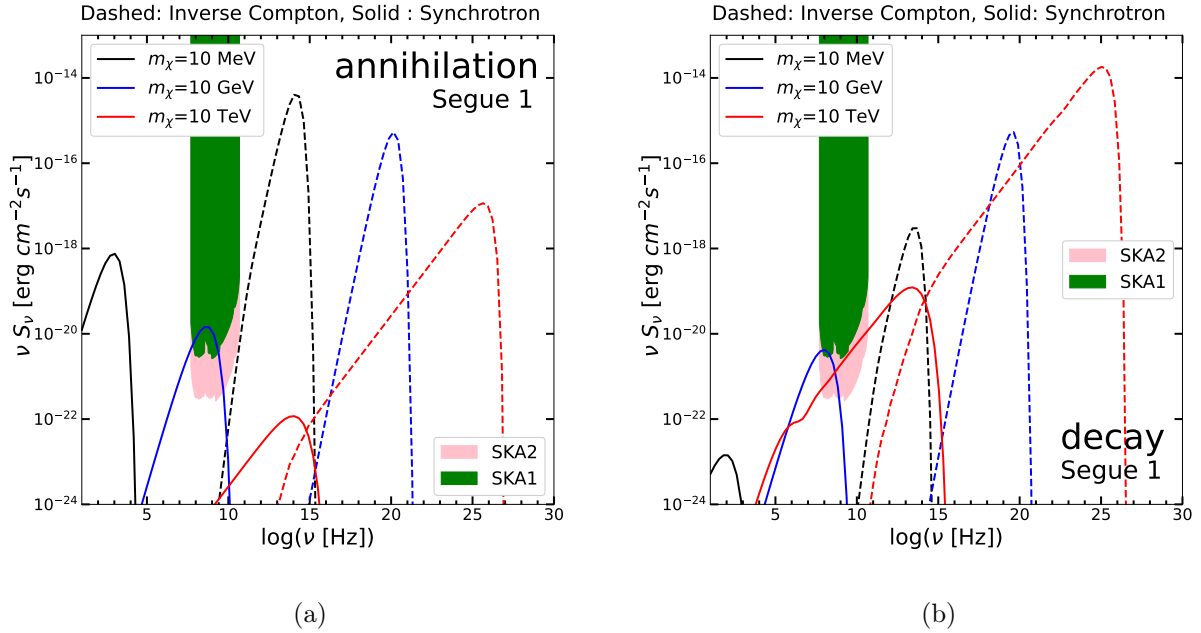


FIG. 1. The energy spectrum distribution from Segue I. The e^+e^- final state are considered and three benchmark DM masses are 10 MeV (blue), 10 GeV (black), and 10 TeV (red). The DM annihilation cross section (left panel) is fixed to be $\langle\sigma v\rangle = 10^{-28} \text{ cm}^3 \text{ s}^{-1}$ while the DM decay time (right panel) is $\tau = 10^{28} \text{ s}$. For DM halo model, we hire the Einasto profile as presentation.

Plugging the green function back to Eq. (6), we can finally write the energy spectrum distribution (SED) for ICS and synchrotron as

$$S_\nu(\nu) = \int d\Omega \int_{l.o.s.} \frac{dl}{4\pi} \int_E^{m_\chi} 2dE \times (\mathcal{P}_{IC} + \mathcal{P}_{syn}) \times \frac{\partial n_e}{\partial E}. \quad (10)$$

The standard power of ICS \mathcal{P}_{IC} and synchrotron \mathcal{P}_{syn} can be found in Ref. [13]. We will see later that the maximum radio frequency of the synchrotron radiation is $\nu \approx 4.7 \text{ GHz}(E/\text{GeV})^2(B/\text{mG})$ while the IC power spectrum \mathcal{P}_{IC} is insensitive by changing the magnetic field [34]. Except clusters, the magnetic field model used in this work is [13]

$$B(r) = B_0 \exp(-r/r_c), \quad (11)$$

where B_0 represents the central magnetic field strength. We adopt the half-light radius as the target center radius r_c . To describe cluster magnetic fields, we adopt the β -model

$$B(r) \propto n_{\text{gas}}(r)^\eta = B_0 \left(1 + \frac{r^2}{r_c^2}\right)^{-(3/2)\beta\eta}, \quad (12)$$

based on the simulation results where cluster magnetic field is a power law of the thermal gas density. The parameter β is fitted by using X-ray data and its value is taken as $\beta = 0.655$ [39, 55]. The β -model well agrees multiple Faraday Rotation Measures of clusters [35]. The best fit values of B_0 and η of A2199 in Faraday Rotation Measures are $B_0 = 11.7 \mu G$ and $\eta = 0.9$ [35, 39].

In Fig. 1, we plot three different masses of the spectrum energy distribution. The projected sensitivity of SKA1 and SKA2 is given by green and pink contours. By assuming Einasto halo profile and e^+e^- final state, the m_χ equal to 10 MeV, 10 GeV, and 10 TeV are represented by black, blue, and red lines, respectively. Here, the DM annihilation cross section in the left panel is $\langle\sigma v\rangle = 10^{-28} \text{ cm}^3\text{s}^{-1}$ while the DM decay rate in the right panel is $\tau = 10^{28} \text{ s}$. We demonstrate the synchrotron contribution by the solid and the ICS one by a dashed line. The diffuse coefficient and magnetic strength are given by $D_0 = 3 \times 10^{28} \text{ cm}^2\text{s}^{-1}$ and $B_0 = 1 \mu G$.

Briefly speaking, ICS contribution dominates at the higher frequency while the synchrotron one does at the lower frequency. For annihilating DM scenario as shown in the left panel of Fig. 1, one can read that only synchrotron emission with $m_\chi \gtrsim \mathcal{O}(1 \text{ GeV})$ or ICS with $m_\chi \lesssim \mathcal{O}(100 \text{ MeV})$ can be probed in the SKA energy range. Similarly, the decaying DM scenario in the right panel of Fig. 1 shows that the DM mass determines the energy distribution ranges. The SKA can only detect the decaying DM scenario via synchrotron (heavy m_χ) or ICS (light m_χ).

There is a tricky feature that appears in the SED of the decaying DM. Unlike the annihilating DM scenario, the SED of the decaying DM is not suppressed by the DM mass so that the heavier DM can generate a higher SED peak. From Eq. (3), one might find the this feature is counterintuitive to the number density ρ/m_χ . On the other hand, the similar factor $(\rho/m_\chi)^2$ in the annihilating DM scenario determines the height of SED peak, despite a nonlinear scaling. Actually, the spectrum $\frac{dN_e}{dE}$ in Eq. (3) is also the function of DM mass and it may play an important role to determine the height of the SED peak. Considering the e^+e^- final state, we find that the 10 TeV DM can decay/annihilate to e^+e^- via the final state radiation which leads to $\frac{dN_e}{dE}$ for the 10 TeV DM around $\mathcal{O}(10^4)$ times higher than the one for the 10 GeV DM. Such an enhanced factor is still not large enough to compensate for the suppressed factor from the number density, 10^{-6} by comparing the 10 TeV annihilating DM to the 10 GeV one. By contrast, the suppressed factor for the 10 TeV decaying DM

is only 10^{-3} which makes the SED of the 10 TeV decaying DM larger than the one of the 10 GeV decaying DM.

In the following subsections, we will demonstrate the impact of the astrophysical uncertainties on the SED of the annihilating DM. The impact of the magnetic strength will be discussed in Sec. III A, the impact of diffusion will be presented in Sec. III B, and the signal strength of SED for different sources will be given in Sec. III C. To demonstrate the astrophysical impacts, we only present our result based on the annihilating DM scenario. It is simply because the relative variation of signal intensity with respect to the magnetic field and diffusion does not much depend on the choice of DM scenario.

A. Impact of the magnetic strength

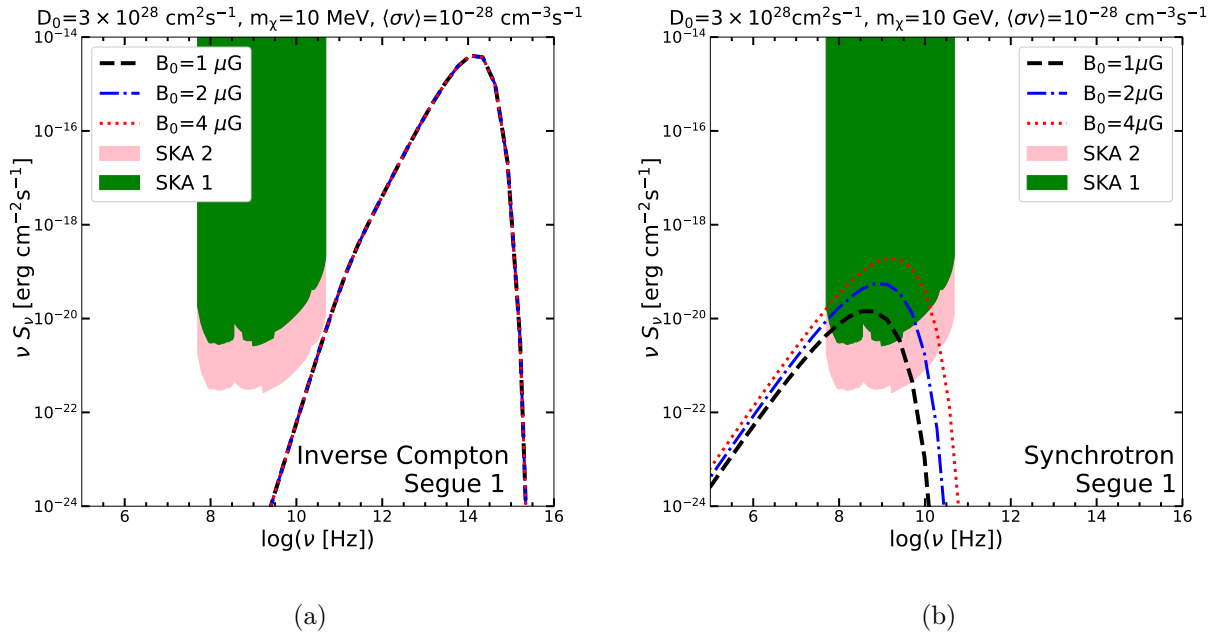


FIG. 2. Comparison of the SED from Segue 1 based on three different B_0 s. Left panel: ICS for $m_\chi = 10 \text{ MeV}$. Right panel: synchrotron for $m_\chi = 10 \text{ GeV}$. Three benchmark values of B_0 are $1 \mu\text{G}$ (black dashed line), $2 \mu\text{G}$ (blue dashed dotted line), and $4 \mu\text{G}$ (red dotted line). The DM is assumed to be annihilating to e^+e^- . The annihilation cross section and the diffusion coefficient are taken as $\langle \sigma v \rangle = 10^{-28} \text{ cm}^3 \text{ s}^{-1}$ and $D_0 = 3 \times 10^{28} \text{ cm}^2 \text{ s}^{-1}$.

The systematic uncertainties of the magnetic strength inside the galaxies remain un-

known. We first discuss the impact of the magnetic strength on the SED and show the SED based on three different B_0 s in Fig. 2 for ICS (left panel) and synchrotron (right panel). We choose the value of the magnetic strength as $1 \mu\text{G}$, $2 \mu\text{G}$, and $4 \mu\text{G}$ presented by black dashed line, blue dashed dotted line, and red dotted line, respectively. Again, we hire Einasto profile as DM halo density. To clearly illustrate the ICS and synchrotron, we show $m_\chi = 10 \text{ MeV}$ for the ICS SED in the left panel but $m_\chi = 10 \text{ GeV}$ for the synchrotron SED in the right panel.

Note that the variation of ICS with respect to the changes of B_0 is negligible but synchrotron contribution is significantly dependent on B_0 . We find that three peaks of the synchrotron energy spectrum are altered non-linearly. This feature comes from two combined effects. First, the mean free path of electrons in Eq. (9) also correlate to the value of the magnetic strength even though their relationship is not as simple as linear re-scaling. Another effect is that the observed radio peak frequency is also increasingly shifted if increasing B_0 . Hence, changing the value of B_0 , one can also alter the shape of the synchrotron SED.

On the other hand, the ICS SED is not sensitive to the change of the magnetic field, because the magnetic field strength inside dSphs is too weak to change ICS SED. Thus, the energy loss term ($B^2 E^2$) is not enough large to make a significant change of ICS SED.

In this work, we simply adopt the magnetic field with the exponential form in Eq. (11) and Eq. (12) which is also the default model in the code of RX-DMFIT [13]. In principle, the magnetic field could be inferred from the density of the star formation rate. However, the extremely low density of dust and gas makes the measurement of polarization difficult so that there are still several choices of the magnetic field model. For example, the magnetic field strength inside Local Group dwarf irregulars could be described by a power law of the density of star formation rate, see [36]. Some recent studies [15, 37] have reported that the center part of the magnetic field strength inside the dSphs is around $1 \mu\text{G}$. However, the spatial distribution of magnetic fields inside the dSphs is still hard to determined [13].

B. Impact of the diffusion coefficient

The diffusion coefficient of cosmic ray propagation is not yet precisely determined. In Fig. 3, we explored the SED of synchrotron and ICS with three possible diffusion coefficients,

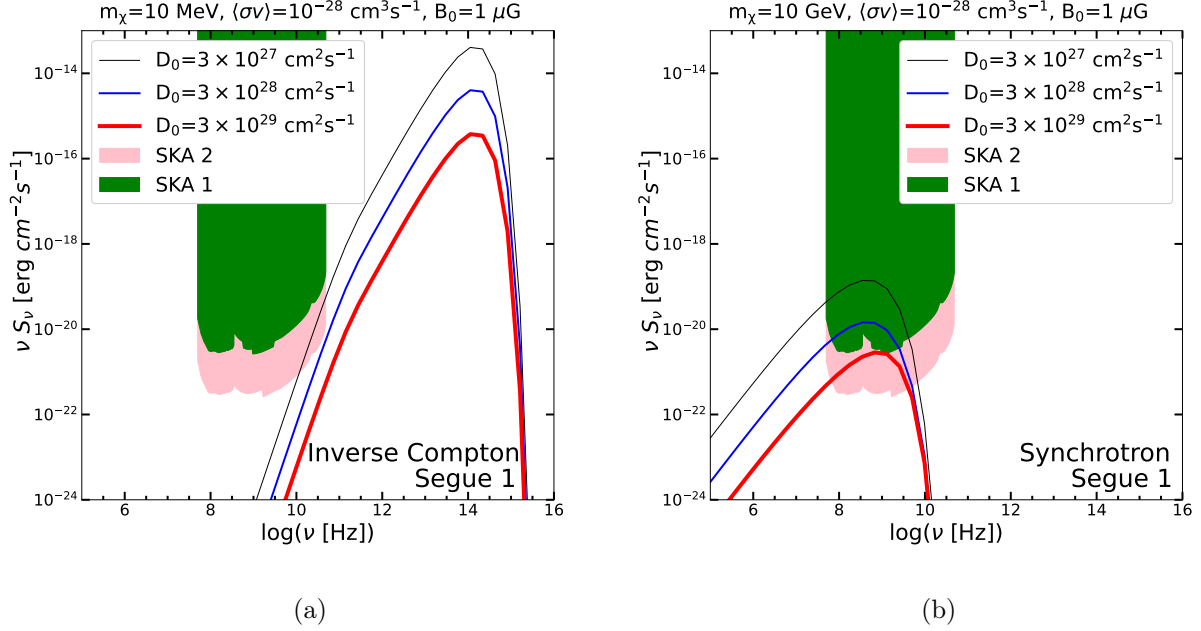


FIG. 3. Variation of SED for Segue 1 with three different D_0 values. The annihilation cross section and magnetic field are fixed as $\langle\sigma v\rangle = 10^{-28} \text{ cm}^3\text{s}^{-1}$ and $B_0 = 1 \mu\text{G}$, respectively. The left panel shows ICS for $m_\chi = 10 \text{ MeV}$. The right panel shows $m_\chi = 10 \text{ GeV}$ for the synchrotron SED. We adopt e^+e^- as our benchmark channel. The red, blue and black lines denote $D_0 = 3 \times 10^{29} \text{ cm}^2\text{s}^{-1}$, $D_0 = 3 \times 10^{28} \text{ cm}^2\text{s}^{-1}$ and $D_0 = 3 \times 10^{27} \text{ cm}^2\text{s}^{-1}$.

$D_0 = 3 \times 10^{27} \text{ cm}^2\text{s}^{-1}$ (black), $D_0 = 3 \times 10^{28} \text{ cm}^2\text{s}^{-1}$ (blue) and $D_0 = 3 \times 10^{29} \text{ cm}^2\text{s}^{-1}$ (red). We employ the Einasto profile as the DM density distribution. We display ICS based on $m_\chi = 10 \text{ MeV}$ (left panel) and synchrotron based on $m_\chi = 10 \text{ GeV}$ (right panel). Here, B_0 is fixed to be $1 \mu\text{G}$ inside Segue 1.

One can see in Fig. 3 that a smaller D_0 can result in a stronger signal strength for both synchrotron radiation and the ICS SED. As long as D_0 is small, the relativistic charged particles can escape from the diffusion zone before producing large energy loss such as synchrotron radiation via galactic magnetic fields or scattering with CMB photons via ICS. Unlike the effect that the magnetic fields determine the peak energy of the SED, the coefficient D_0 is only related to the height of the SED. As for completeness, in the result section, we will present the sensitivities of SKA1 and SKA2 by taking three D_0 s together with three B_0 s as a systematic study.

	Draco [13]	Segue 1 [16, 38]	A2199 [39–41]	DF44 [42]
Distance from the Earth l_0	80 kpc	23 kpc	118 Mpc	101 Mpc
r_h (kpc)	2.5	1.6	500.0	9.2
r_{core} (kpc)	0.22	0.038	102	4.6
B_0 (μG)	1.0	1.0	11.7	1.0
ρ_s (GeV/cm^3)	1.4	6.6	0.0854	0.107
r_s (kpc)	1.0	0.15	340	9.27
D_0 (cm^2s^{-1})	3×10^{28}	3×10^{28}	3×10^{28}	3×10^{28}
Angular size (deg)	1.79	4.0	0.24	0.0052
Halo profile	NFW	Einasto	NFW	NFW

TABLE I. The preference values of model parameters for Draco, Segue 1, A2199 and Dragonfly 44 (DF44).

C. Survey of different sources

Intuitively, we can choose the brightest source to set a most stringent limit on DM annihilation cross section $\langle\sigma v\rangle$ or DM decay time τ . However, different sources have various magnetic field strengths, DM halo distribution, and the distance to the Earth. From Eq. (10), we can read that those various source properties may constrain DM parameter space differently. Therefore, we compare the SED from four different sources as their properties summarized in table I. We focus on two dSphs (Draco and Segue 1), one radio-poor cluster (A2199), and one DM rich ultra-diffuse galaxy (Dragonfly 44).

The angular size is defined by $\alpha = \arctan(r/l_0)$, where l_0 is the distance from the Earth to the target and r is the target radius of region of interest. We evaluate the values of diffusion zone α for four sources are 1.79 deg (Draco), 4.0 deg (Segue 1), 0.24 deg (A2199), and 0.0052 deg (DF44). The SKA has wide field-of-view (FOV) receivers and can use multiple FOVs to observe the entire sky. The FoV is inversely proportional to frequency-square. The values of FOV at different frequencies are: 327 arcmin at 150 MHz, 120 arcmin at 300 MHz, 109 arcmin at 770 MHz, 60 arcmin at 1.4 GHz, 12.5 arcmin at 6.7 GHz and 6.7 arcmin at 12.5 GHz [29]. When driving a very conservative sensitivity, one could require α within a FOV. However, the SKA allows us to digitally patch several FOVs in order to cover our

interesting angular size.

Although the magnetic field strength B_0 in M31 can be a large value $15 \pm 3 \mu\text{G}$ determined by the Faraday rotation measurement of polarized radio emissions, searching for DM induced synchrotron from M31 can be contaminated by the background radio of M31. Instead, we select a radio poor cluster A2199 as an example. Yet, the diffuse radio emission from A2199 is still detected as an upper limit at 327 MHz by the Westerbork Northern Sky Survey [49]. Furthermore, recent observation has reported that Dragonfly 44 (DF44) is one of the largest ultra-diffuse galaxies (UDGs) in the Coma cluster and it is very dark with a high mass-to-light ratio around $48_{-14}^{+21} M_\odot/L_\odot$ [43]. Namely, around 99% of total DF44 mass is DM. We simply fix the value of B_0 inside the DF44 as $1 \mu\text{G}$ because the magnetic field in clusters can be estimated around $0.1 - 1 \mu\text{G}$ based on the observation of radio halos [44]. Also, we can search DM radio emission from other DM rich system like dSphs. Here, we take Draco as a classic option while Segue 1 is the nearest dSph to the Earth.

For DM density distribution, we choose the NFW profile for Draco, A2199, and DF44. However, the NFW profile can not fit the rotation velocity data of Segue 1 well. Hence, we adopt Einasto profile with $\alpha = 0.3$ for Segue 1 [16]. Regarding the diffusing coefficient, we simply take a typical value $D_0 = 3 \times 10^{28} \text{cm}^2 \text{s}^{-1}$ for all the sources.

Fig. 4 demonstrates the DM SED from four different sources (Draco, Segue 1, A2199 and DF44) generated through ICS (left panel) and synchrotron emission (right panel). Again, we compute both DM induced ICS and synchrotron with a fixed annihilation cross section $\langle\sigma v\rangle = 10^{-28} \text{cm}^3 \text{s}^{-1}$ while DM mass is 10 MeV for ICS but 10 GeV for synchrotron emission. From the right panel of Fig. 4, we found that DM induced ICS is basically governed by the propagation distance from the source to the Earth so that the predicted SED from Segue 1 is the largest and the one from DF44 is the smallest among these four chosen sources. This can be understood by the fact that ICS is not sensitive to B_0 as shown in Fig. 2 but the flux is inversely proportional to the square of the distance, even if the size of DF44 is much larger than Segue 1. *Hence, Segue 1 is the best source for searching DM induced ICS among these four selected sources.*

On the other hand, the DM SED generated through synchrotron emission behaves more non-trivially. The combined effects from the distance from the Earth, halo size, and B_0 make Segue 1 less detectable than Draco and A2199. The relative strength between these four sources can be partially determined by the distance from the Earth. Still, one can tell

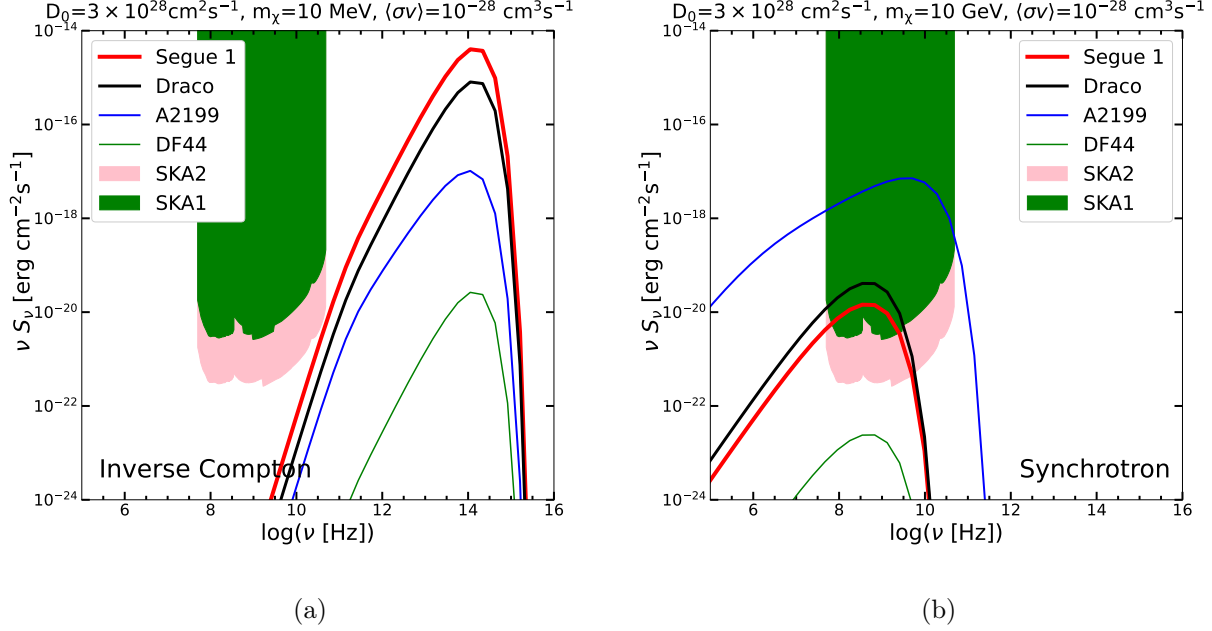


FIG. 4. The DM energy spectra from different sources by assuming a e^+e^- channel. The left panel is ICS SED for $m_\chi = 10$ MeV while the right panel displays synchrotron SED for $m_\chi = 10$ GeV. We compare the following four sources: Draco, Segue 1, A2199, and DF44.

that the magnetic field B_0 partially determines the SED strength. In addition, we learn from Fig. 2 that DM SED can widely spread within a large B_0 source. For example, the SED from A2199 is peaked at around 10^9 Hz but the one from Segue 1 is peaked at around 3×10^8 Hz. *For detecting the DM SED generated through synchrotron, A2199 can be more promising than others.*

IV. RESULT

In this section, by using Eq. (1), we project the minimum SKA1 and SKA2 flux to $(m_\chi, \langle\sigma v\rangle)$ plane for DM annihilation scenario but to (m_χ, τ) for DM decay one. To include the systematic uncertainties, we adopt three benchmarks, $D_0/10^{28}/(\text{cm}^2\text{s}^{-1}) = 30, 3, 0.3$. For magnetic field B_0 , it depends on the selected source. As discussed in Sec. III C, the most promising source for DM ICS is Segue 1 while the one for DM synchrotron is A2199. Therefore, we present SKA1 and SKA2 limits based on these two sources. Finally, we can define three benchmarks based on six combinations of B_0 and D_0 ,

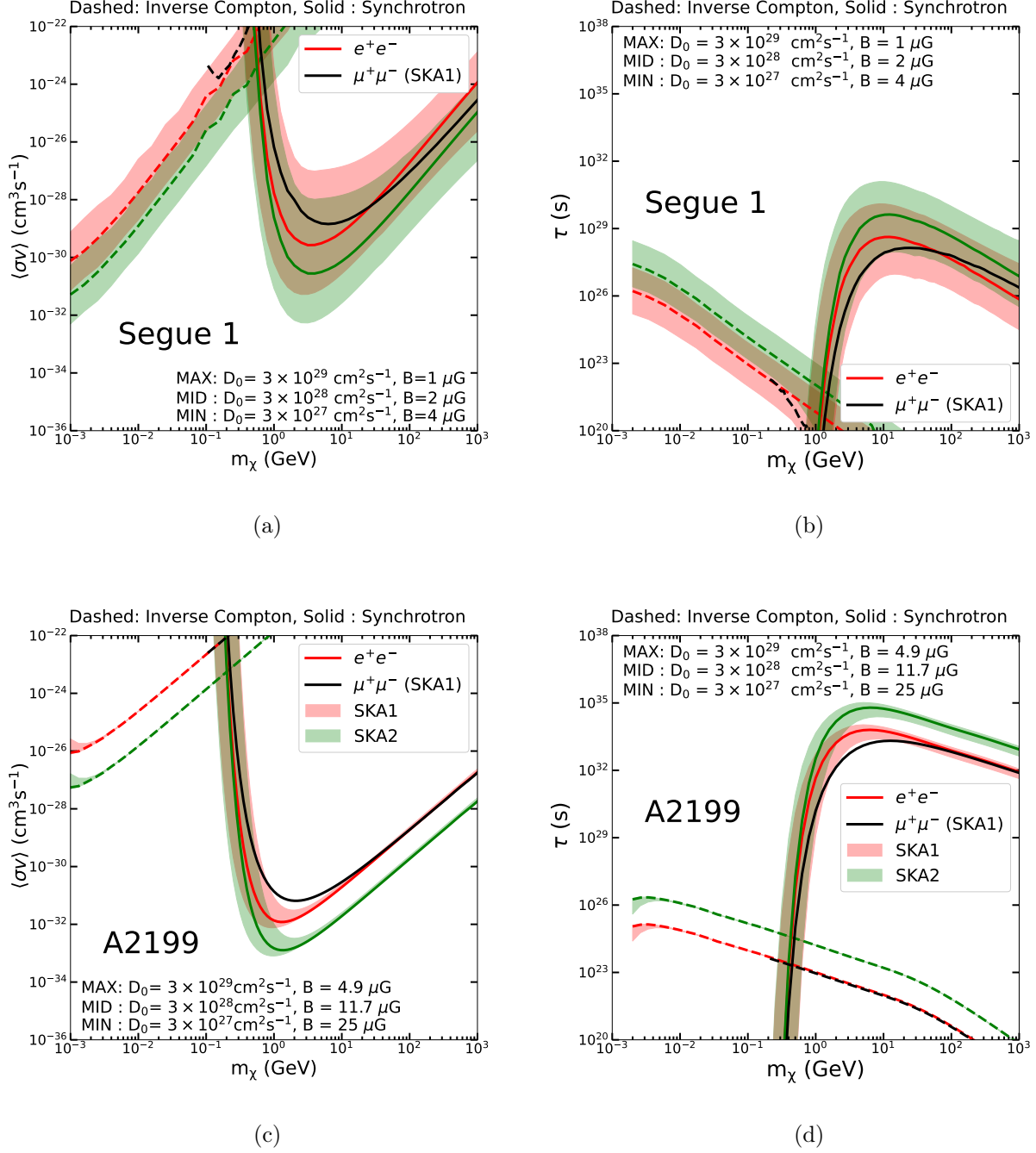


FIG. 5. The upper limits of DM annihilation cross section $\langle\sigma v\rangle$ (two left panels) and the lower limits DM decay time τ (two right panels) based on SKA1 (red bands) and SKA2 (green bands) with 100 hours of exposure. The two upper and lower panels represent the limits from Segue 1 and A2199, respectively. Except for B_0 and D_0 , the rest configurations of Segue and A2199 are given in table I. The upper edge, central line, and lower edge of pink and green bands correspond to the configuration of MAX, MID, and MIN. The dash lines show the limits from DM induced ICS and the solid lines denote the limits from DM induced synchrotron fluxes.

- MAX: $D_0 = 3 \times 10^{29} \text{ cm}^2\text{s}^{-1}$ and B_0^{MAX} ,
- MID: $D_0 = 3 \times 10^{28} \text{ cm}^2\text{s}^{-1}$ and B_0^{MID} ,
- MIN: $D_0 = 3 \times 10^{27} \text{ cm}^2\text{s}^{-1}$ and B_0^{MIN} .

Here, the selected three benchmark B_0^{MAX} , B_0^{MID} , and B_0^{MIN} are $B_0/\mu\text{G} = 1.0, 2.0, 4.0$ for Segue 1 but $B_0/\mu\text{G} = 4.9, 11.7, 25$ for A2199.

In Fig. 5, We show our derived upper limits of $\langle\sigma v\rangle$ (two panels in the left column) and the lower limits of τ (two panels in the right column). The two upper panels are based on Segue 1 but the two lower panels are based on A2199. We depict the sensitivities of SKA1 and SKA2 for e^+e^- final state as a red and green band, respectively. The upper and lower edges correspond to MIN and MAX configuration. In comparison, the black solid line is the SKA1 sensitivity for $\mu^+\mu^-$ final state. We note that the limits based on e^+e^- and $\mu^+\mu^-$ final state only differ near the threshold.

For the DM annihilation scenario, the upper limits (Segue 1) are governed by DM induced ICS at $m_\chi \lesssim 0.4 \text{ GeV}$ but DM induced synchrotron emission at $m_\chi \gtrsim 0.4 \text{ GeV}$. However, the crossing point of two contributions is shifted to $m_\chi \approx 0.8 \text{ GeV}$ if the decaying DM is considered. We can see that the limits at DM mass heavier than 1 TeV can be simply obtained by linear extrapolation. Comparing the limits from Segue 1 (two upper panels) and A2199 (two lower panels), the spreads of limits from these three benchmark configurations are roughly three orders for Segue 1 but the color bends for A2199 is much shrunk. This is because diffusion zone radius r_h of A2199 is much larger than the one of Segue 1. Using the same diffusion coefficient, the electrons and positrons in A2199 are more likely confined within r_h than in Segue 1. Moreover, we also learn that the systematic uncertainties are overwhelmed by B_0 than the one from D_0 .

By combining the result from Segue 1 and A2199, for e^+e^- final state we expect the future SKA1 can probe the region $\langle\sigma v\rangle \gtrsim 10^{-32} \text{ cm}^3\text{s}^{-1}$ for annihilating DM and $\tau \gtrsim 10^{34} \text{ s}$ for decaying DM at $m_\chi \simeq 1 \text{ GeV}$. For $\mu^+\mu^-$ final state, the limits are weaker about one order magnitude than the former. The limits will be further improved by SKA2 by around one order magnitudes. Strikingly, this is a piece of good news for the annihilating DM scenario because the SKA may offer a chance to detect a very low DM annihilation cross section in the present universe, for example DM annihilation only via p -wave or off-resonance at the present.

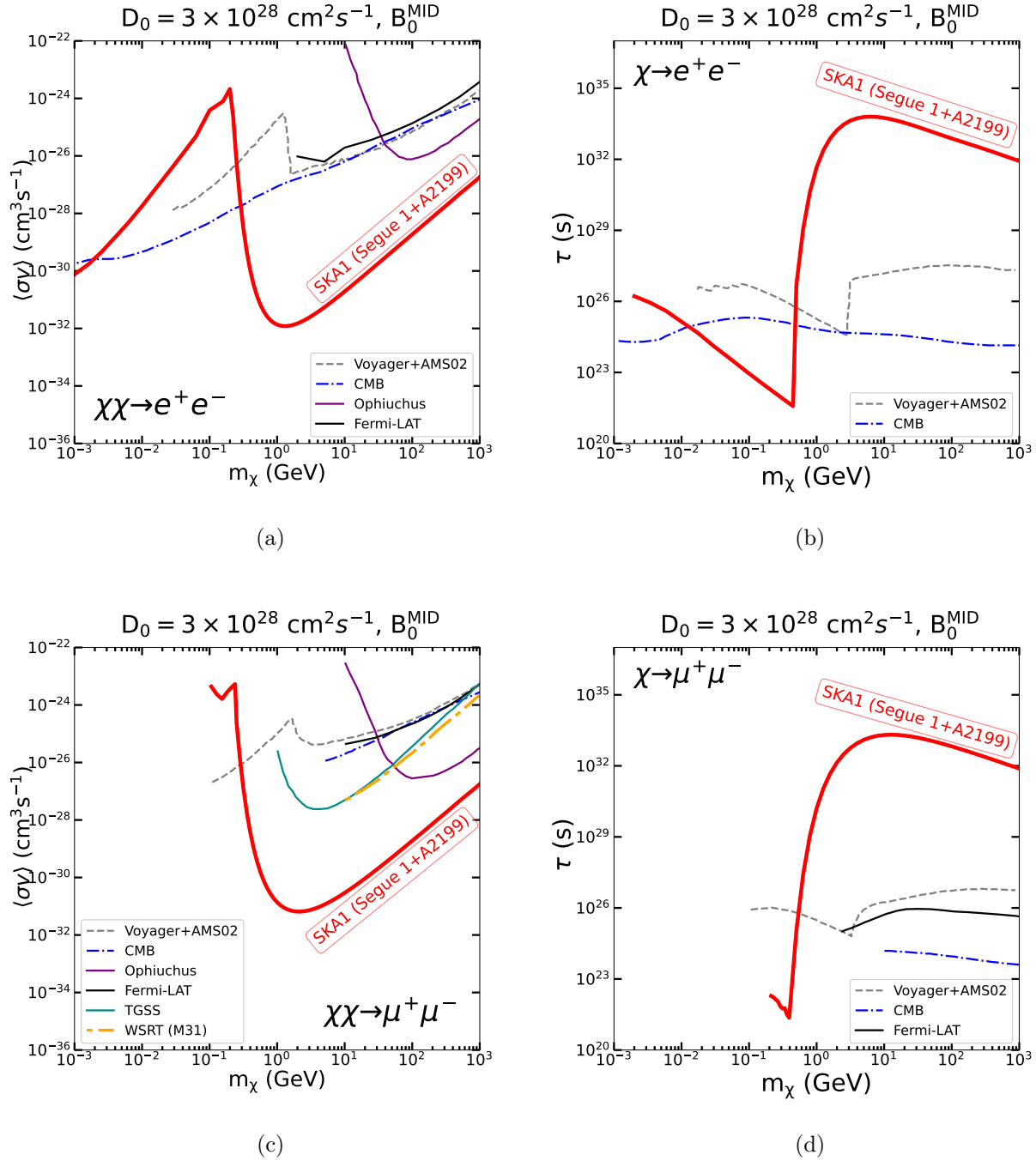


FIG. 6. Comparisons with other existing limits based on e^+e^- (upper panels) and $\mu^+\mu^-$ (lower panels) final state. The annihilating and decaying DM scenarios are shown in the right and left panels. We plot the SKA1 limit with MID configuration as the red lines where we combine two limits from ICS at the small m_χ region of Segue 1 and synchrotron emission at the large m_χ region of A2199.

Finally, we compare our results with other previous existing limits in Fig. 6 by choosing the e^+e^- (upper panels) and $\mu^+\mu^-$ (lower panels) final state. The limits of Ophiuchus from VLA are shown by purple lines [50, 51]. The stacking analysis of 23 dSph galaxies [18] is indicated by darkcyan solid lines (TGSS). The orange long dashed line is taken from [46] which uses the M31 result from the Westerbork Synthesis Radio Telescope (WSRT) [45]. The limits obtained by CMB data and Voyager and AMS02 data are shown by blue dash-dotted lines and gray dash lines [52–54]. The limit of Fermi LAT [47, 48] is also given by thin black lines. Here, we show SKA1 limits by combining the result from DM induced ICS and synchrotron emission. The limit for the large m_χ region is obtained by using DM induced synchrotron emission with the source configuration Segue 1 MID. On the other hand, the limit for the small m_χ region is based on the ICS one with the source configuration A2199 MID. The crossing point between the large and small m_χ region is at $m_\chi \approx 0.2$ GeV for annihilating DM but $m_\chi \approx 0.4$ GeV for decaying DM. We can see that the current limits from dSphs are approximately four order magnitude (annihilating DM) and six order magnitude (decaying DM) weaker than the future SKA1 sensitivity at the heavy DM mass region. Our limits are also two orders of magnitude stronger than VLA Ophiuchus limits. However, if only considering Segue 1 as a comparison, SKA1 limits could be stronger than current dSphs limits by one order magnitude for both DM scenarios. For the region near the detector threshold $m_\chi < 10$ GeV, the SKA shows its capability in detecting the low mass region.

V. SUMMARY

In this work, we systematically study the future SKA detectability of MeV to TeV DM annihilation or decay signal. The detected frequency of radio in the SKA is between 50 MHz to 50 GHz. Within the required range, e^+e^- can emit radio depending on their energies. First, the relativistic e^+e^- whose kinetic energies are larger than $\mathcal{O}(100$ MeV) can emit radio via synchrotron with the galactic magnetic field. On the other hand, a soft e^+e^- spectrum with kinetic energies less than $\mathcal{O}(100$ MeV) can only produce radio via ICS with CMB photons. Thus, the radio emission falling to the SKA detected frequency range generated via DM induced ICS or synchrotron requires DM mass lighter or heavier than $\mathcal{O}(100-200)$ MeV, respectively. To set an upper limit on DM annihilation cross section or a lower limit on decay time, we consider both SED of DM induced ICS and synchrotron by comparing with the

minimum flux of two SKA phases (SKA1 and SKA2).

We compute the both SED of DM induced ICS and synchrotron based on several selected values of magnetic field strength B_0 and diffusion coefficient D_0 . By using $m_\chi = 10$ MeV for ICS and $m_\chi = 10$ GeV for synchrotron, we again confirm that the impact of different B_0 on SED is more important for synchrotron than ICS. When changing to a larger value of B_0 , not only the SED of DM induced synchrotron can be enhanced but also its peak is shifted to a larger frequency. However, changing to a larger value of B_0 only alters the SED of DM induced ICS insignificantly. Moreover, if varying the value of D_0 , we note that both ICS and synchrotron SED are also modified accordingly.

We then attempt to figure out which source could be the best target for DM search based on the SKA sensitivity and frequency range. To perform a comparison, we select four different sources: Draco, Segue 1, A2199, and DF44. Here, A2199 is a radio-poor cluster, DF44 is a DM-rich ultra-diffuse galaxy, but Draco and Segue 1 are dSphs. Since DM induced ICS does not sensitive to B_0 , the closer source is better for the SKA observation. Therefore, we found Segue 1 is the best source of searching for MeV scale DM among these four sources. However, DM induced synchrotron is more complicated because of the combined effects from different B_0 and the distance from the Earth. In the end, we conclude that the A2199 is a more promising source than others for $m_\chi \gtrsim \mathcal{O}(\text{GeV})$ because of its largest B_0 even if it is further than others.

After presenting the SED changes based on different values of B_0 and D_0 as well as using different sources, we finally select three different benchmark configurations of B_0 and D_0 . Based on these three representative configurations (MAX, MID, and MIN), we project the sensitivity of SKA1 and SKA2 to $(m_\chi, \langle\sigma v\rangle)$ for annihilating DM scenario and (m_χ, τ) for decaying DM scenario by choosing e^+e^- and $\mu^+\mu^-$ final states as demonstration. From MeV to TeV DM mass, the most stringent limit appears at around GeV where DM induced synchrotron still dominates at the SKA detected frequency range.

Comparing with other studies of DM radio probes with the future SKA sensitivity, our work includes three new differences. First, we compute the minimum fluxes by using a frequency-dependent bandwidth. The resulted limits on DM interaction can be slightly stronger than the ones used a frequency-independent bandwidth. Second, we study DM induced radio signals including ICS and synchrotron emission. By utilizing both DM contributions, we calculate the SKA sensitivity at the DM mass gap between 100 MeV to 5 GeV.

Third, it is the first time to study DM rich ultra-diffuse galaxy DF44 with SKA sensitivity. Our result shows that the DM SED from DF44 is the lowest among the four selected sources.

We also compared the projected SKA1 limits with other current limits of annihilation cross section and decay time in Fig. 6. We found that the SKA projected limit is much stronger than other previous exist limits from various DM indirect detectors, even only considering the SKA phase 1 sensitivity. At the heavy DM mass region where synchrotron contribution is dominant, the current most stringent limits such as TGSS at $m_\chi \sim 1$ GeV ($\mu^+\mu^-$) and VLA Ophiuchus limit at $m_\chi \sim 1$ TeV (e^+e^- and $\mu^+\mu^-$) are both weaker than the SKA1 sensitivity. Taking the e^+e^- final state as example, the SKA1 limit shows that $\langle\sigma v\rangle$ can be as lower as 10^{-32} cm^3s^{-1} and τ can be 10^{34} s at $m_\chi = 1$ GeV but they become $\langle\sigma v\rangle \lesssim 10^{-27}$ cm^3s^{-1} and $\tau \gtrsim 10^{32}$ s at $m_\chi = 1$ TeV, based on the A2199 MID configuration. For $m_\chi = 5$ MeV, the SKA1 limits derived from ICS inside Segue 1 with MID configuration are $\langle\sigma v\rangle \lesssim 10^{-29}$ cm^3s^{-1} and $\tau \gtrsim 10^{26}$ s . If the final state is e^+e^- , the present CMB can set a very stringent limit in the low DM mass region but the SKA1 projected limit from DM induced ICS can be still stronger at the region $m_\chi \lesssim 10$ MeV.

In summary, we compare the SKA1 sensitivity with current existing limits as shown in Fig. 6. The limits of $\langle\sigma v\rangle$ and τ can be significantly improved by the future SKA1 and this will help us to probe a large of the DM parameter space. For DM with velocity dependent annihilation cross section, e.g. annihilation only with p -wave suppressed cross section or annihilation via resonance in the early universe, the SKA would play a leading role to explore such DM models.

ACKNOWLEDGMENTS

We thank an anonymous referee for useful comments on SKA sensitivity. Zhanfang Chen would like to thank Xu Pan for his valuable comments and discussions. Q. Yuan is supported by the National Natural Science Foundation of China under Grant No. U1738205, Chinese Academy of Sciences, and the Program for Innovative Talents and Entrepreneur in Jiangsu.

[1] J. Liu, X. Chen and X. Ji, Nature Phys. **13** (2017) no.3, 212-216 doi:10.1038/nphys4039 [arXiv:1709.00688 [astro-ph.CO]].

- [2] M. Schumann, *J. Phys. G* **46** (2019) no.10, 103003 doi:10.1088/1361-6471/ab2ea5 [arXiv:1903.03026 [astro-ph.CO]].
- [3] O. Buchmueller, C. Doglioni and L. T. Wang, *Nature Phys.* **13** (2017) no.3, 217-223 doi:10.1038/nphys4054 [arXiv:1912.12739 [hep-ex]].
- [4] F. Kahlhoefer, *Int. J. Mod. Phys. A* **32** (2017) no.13, 1730006 doi:10.1142/S0217751X1730006X [arXiv:1702.02430 [hep-ph]].
- [5] R. K. Leane, [arXiv:2006.00513 [hep-ph]].
- [6] J. M. Gaskins, *Contemp. Phys.* **57** (2016) no.4, 496-525 doi:10.1080/00107514.2016.1175160 [arXiv:1604.00014 [astro-ph.HE]].
- [7] C. Pérez de los Heros, *Symmetry* **12** (2020) no.10, 1648 doi:10.3390/sym12101648 [arXiv:2008.11561 [astro-ph.HE]].
- [8] A. Albert *et al.* [Fermi-LAT and DES], *Astrophys. J.* **834** (2017) no.2, 110 doi:10.3847/1538-4357/834/2/110 [arXiv:1611.03184 [astro-ph.HE]].
- [9] H. Abdallah *et al.* [H.E.S.S.], *Phys. Rev. Lett.* **117** (2016) no.11, 111301 doi:10.1103/PhysRevLett.117.111301 [arXiv:1607.08142 [astro-ph.HE]].
- [10] H. Silverwood, C. Weniger, P. Scott and G. Bertone, *JCAP* **03** (2015), 055 doi:10.1088/1475-7516/2015/03/055 [arXiv:1408.4131 [astro-ph.HE]].
- [11] S. Colafrancesco, S. Profumo and P. Ullio, *Astron. Astrophys.* **455** (2006), 21 doi:10.1051/0004-6361:20053887 [arXiv:astro-ph/0507575 [astro-ph]].
- [12] K. Spekkens, B. S. Mason, J. E. Aguirre and B. Nhan, *Astrophys. J.* **773** (2013), 61 doi:10.1088/0004-637X/773/1/61 [arXiv:1301.5306 [astro-ph.CO]].
- [13] A. McDaniel, T. Jeltema, S. Profumo and E. Storm, *JCAP* **09** (2017), 027 doi:10.1088/1475-7516/2017/09/027 [arXiv:1705.09384 [astro-ph.HE]].
- [14] B. Dutta, A. Kar and L. E. Strigari, *JCAP* **03** (2021), 011 doi:10.1088/1475-7516/2021/03/011 [arXiv:2010.05977 [astro-ph.HE]].
- [15] M. Regis, L. Richter and S. Colafrancesco, *JCAP* **07** (2017), 025 doi:10.1088/1475-7516/2017/07/025 [arXiv:1703.09921 [astro-ph.HE]].
- [16] A. Natarajan, J. E. Aguirre, K. Spekkens and B. S. Mason, [arXiv:1507.03589 [astro-ph.CO]].
- [17] A. Kar, S. Mitra, B. Mukhopadhyaya, T. R. Choudhury and S. Tingay, *Phys. Rev. D* **100** (2019) no.4, 043002 doi:10.1103/PhysRevD.100.043002 [arXiv:1907.00979 [astro-ph.HE]].

- [18] A. Basu, N. Roy, S. Choudhuri, K. K. Datta and D. Sarkar, *Mon. Not. Roy. Astron. Soc.* **502** (2021) no.2, 1605-1611 doi:10.1093/mnras/stab120 [arXiv:2101.04925 [astro-ph.HE]].
- [19] A. Kar, S. Mitra, B. Mukhopadhyaya and T. R. Choudhury, *Phys. Rev. D* **101** (2020) no.2, 023015 doi:10.1103/PhysRevD.101.023015 [arXiv:1905.11426 [hep-ph]].
- [20] J. A. R. Cembranos, Á. De La Cruz-Dombriz, V. Gammaldi and M. Méndez-Isla, *Phys. Dark Univ.* **27** (2020), 100448 doi:10.1016/j.dark.2019.100448 [arXiv:1905.11154 [hep-ph]].
- [21] G. Beck, M. Kumar, E. Malwa, B. Mellado and R. Temo, [arXiv:2102.10596 [astro-ph.HE]].
- [22] S. von Buddenbrock, A. S. Cornell, A. Fadol, M. Kumar, B. Mellado and X. Ruan, *J. Phys. G* **45** (2018) no.11, 115003 doi:10.1088/1361-6471/aae3d6 [arXiv:1711.07874 [hep-ph]].
- [23] P. Bhattacharjee, D. Choudhury, K. Das, D. K. Ghosh and P. Majumdar, [arXiv:2011.08917 [hep-ph]].
- [24] S. Colafrancesco, P. Marchegiani and G. Beck, *JCAP* **02** (2015), 032 doi:10.1088/1475-7516/2015/02/032 [arXiv:1409.4691 [astro-ph.CO]].
- [25] A. Kar, S. Mitra, B. Mukhopadhyaya and T. R. Choudhury, *Phys. Rev. D* **99** (2019) no.2, 021302 doi:10.1103/PhysRevD.99.021302 [arXiv:1808.05793 [hep-ph]].
- [26] A. Ghosh, A. Kar and B. Mukhopadhyaya, *JCAP* **09** (2020), 003 doi:10.1088/1475-7516/2020/09/003 [arXiv:2001.08235 [hep-ph]].
- [27] P. Dewdney, W. Turner, R. Millenaar, R. McCool, J. Lazio, and T. Cornwell. Ska1 system baseline design. *Document number SKA-TEL-SKO-DD-001 Revision*, 1(1), 2013.
- [28] R. Braun, A. Bonaldi, T. Bourke, E.F. Keane, and J. Wagg. Anticipated ska1 science performance. *SKA-TEL-SKO-0000818*, 2017.
- [29] R. Braun, A. Bonaldi, T. Bourke, E. Keane and J. Wagg, [arXiv:1912.12699 [astro-ph.IM]].
- [30] D. Maurin, F. Donato, R. Taillet and P. Salati, *Astrophys. J.* **555** (2001), 585-596 doi:10.1086/321496 [arXiv:astro-ph/0101231 [astro-ph]].
- [31] W. R. Webber, M. A. Lee and M. Gupta, *Astrophys. J.* **390** (1992), 96 doi:10.1086/171262
- [32] S. Colafrancesco, S. Profumo and P. Ullio, *Phys. Rev. D* **75**, 023513 (2007) doi:10.1103/PhysRevD.75.023513 [arXiv:astro-ph/0607073 [astro-ph]].
- [33] M. Vollmann, doi:10.1088/1475-7516/2021/04/068 [arXiv:2011.11947 [astro-ph.HE]].
- [34] Profumo S., Ullio P., 2010, *Particle Dark Matter: Observations, Models and Searches*, ed. G. Bertone, Cambridge University Press, chapter 27.

- [35] Vacca V., Murgia M., Govoni F., Feretti L., Giovannini G., Perley R. A., Taylor G. B., 2012, *A&A*, 540, A38. doi:10.1051/0004-6361/201116622
- [36] K. T. Chyzy, M. Wezgowiec, R. Beck and D. J. Bomans, *Astron. Astrophys.* **529** (2011), A94 doi:10.1051/0004-6361/201015393 [arXiv:1101.4647 [astro-ph.CO]].
- [37] M. Regis, S. Colafrancesco, S. Profumo, W. J. G. de Blok, M. Massardi and L. Richter, *JCAP* **10** (2014), 016 doi:10.1088/1475-7516/2014/10/016 [arXiv:1407.4948 [astro-ph.CO]].
- [38] J. D. Simon, M. Geha, Q. E. Minor, G. D. Martinez, E. N. Kirby, J. S. Bullock, M. Kaplinghat, L. E. Strigari, B. Willman and P. I. Choi, *et al.* *Astrophys. J.* **733** (2011), 46 doi:10.1088/0004-637X/733/1/46 [arXiv:1007.4198 [astro-ph.GA]].
- [39] E. Storm, T. E. Jeltema, S. Profumo and L. Rudnick, *Astrophys. J.* **768** (2013), 106 doi:10.1088/0004-637X/768/2/106 [arXiv:1210.0872 [astro-ph.CO]].
- [40] A. M. Groener, D. M. Goldberg and M. Sereno, *Mon. Not. Roy. Astron. Soc.* **455**, no.1, 892-919 (2016) doi:10.1093/mnras/stv2341 [arXiv:1510.01961 [astro-ph.CO]].
- [41] Babyk, I. V., Del Popolo, A., & Vavilova, I. B. 2014, *Astronomy Reports*, 58, 587. doi:10.1134/S1063772914090017
- [42] A. Wasserman, P. van Dokkum, A. J. Romanowsky, J. Brodie, S. Danieli, D. A. Forbes, R. Abraham, C. Martin, M. Matuszewski and A. Villaume, *et al.* doi:10.3847/1538-4357/ab3eb9 [arXiv:1905.10373 [astro-ph.GA]].
- [43] P. van Dokkum, R. Abraham, J. Brodie, C. Conroy, S. Danieli, A. Merritt, L. Mowla, A. Romanowsky and J. Zhang, *Astrophys. J. Lett.* **828** (2016) no.1, L6 doi:10.3847/2041-8205/828/1/L6 [arXiv:1606.06291 [astro-ph.GA]].
- [44] C. L. Carilli and G. B. Taylor, *Ann. Rev. Astron. Astrophys.* **40** (2002), 319-348 doi:10.1146/annurev.astro.40.060401.093852 [arXiv:astro-ph/0110655 [astro-ph]].
- [45] R. Gießübel, G. Heald and R. Beck, *Astron. Astrophys.* **559** (2013), A27 doi:10.1051/0004-6361/201321765 [arXiv:1309.2539 [astro-ph.CO]].
- [46] M. H. Chan, *Phys. Rev. D* **94** (2016) no.2, 023507 doi:10.1103/PhysRevD.94.023507 [arXiv:1606.08537 [astro-ph.HE]].
- [47] M. G. Baring, T. Ghosh, F. S. Queiroz and K. Sinha, *Phys. Rev. D* **93** (2016) no.10, 103009 doi:10.1103/PhysRevD.93.103009 [arXiv:1510.00389 [hep-ph]].
- [48] M. Ackermann *et al.* [Fermi-LAT], *Phys. Rev. Lett.* **115** (2015) no.23, 231301 doi:10.1103/PhysRevLett.115.231301 [arXiv:1503.02641 [astro-ph.HE]].

- [49] Rudnick, L. & Lemmerman, J. A. 2009, *Astrophys. J.*, 697, 1341. doi:10.1088/0004-637X/697/2/1341
- [50] Murgia M., Eckert D., Govoni F., Ferrari C., Pandey-Pommier M., Nevalainen J., Paltani S., 2010, *A&A*, 514, A76. doi:10.1051/0004-6361/201014126
- [51] Beck G., 2020, *MNRAS*, 494, 1128. doi:10.1093/mnras/staa806
- [52] J. Cang, Y. Gao and Y. Z. Ma, *Phys. Rev. D* **102**, no.10, 103005 (2020) doi:10.1103/PhysRevD.102.103005 [arXiv:2002.03380 [astro-ph.CO]].
- [53] T. R. Slatyer and C. L. Wu, *Phys. Rev. D* **95**, no.2, 023010 (2017) doi:10.1103/PhysRevD.95.023010 [arXiv:1610.06933 [astro-ph.CO]].
- [54] M. Boudaud, J. Lavalle and P. Salati, *Phys. Rev. Lett.* **119**, no.2, 021103 (2017) doi:10.1103/PhysRevLett.119.021103 [arXiv:1612.07698 [astro-ph.HE]].
- [55] Bonafede A., Feretti L., Murgia M., Govoni F., Giovannini G., Dallacasa D., Dolag K., et al., 2010, *A&A*, 513, A30. doi:10.1051/0004-6361/200913696